Numerical investigation of two-phase flows in highly-permeable porous media: Effect of the permeability on the drag force between fluid phases

Maxime Cochennec, Hossein Davarzani, Yoahn Davit, Michel Quintard

Abstract

The macroscopic description of two-phase flows in porous media requires accurate modelling of the drag forces between the two fluids and the solid phase. In standard porous media, where capillarity is often dominant, the fluid-solid interactions are well-known and the fluid-fluid drag force is treated in a similar way as the drag between fluids and solid in the momentum transport equation. Two-phase flows in highly permeable porous media, however, are often characterized by a larger area of the interface between the two fluids and the development of thin films. In such cases, the fluid-fluid interaction is not necessarily negligible and may play an important role in the momentum transport equations. Here, we use computational methods to study two-phase flows in a microfluidic device made of an array of cylinders squeezed between two plates in a Hele-Shaw flow cell. The idea is to keep the geometry in the cell plane unmodified whereas the aperture h between the plates is changed to explore different ranges of permeability. This is done by solving depth-averaged flow equations, taking advantage of the quasi-planar nature of the flow. We reproduce a film-flow regime and show that the fluid-fluid drag is non-negligible as it reaches between 5% and 60% of the solid-fluid drag. XXXOur results demonstrate that the fluid-fluid drag force should not be neglected in momentum transport equations and behaves differently than the drag upon solids, confirming that a no-flow condition between fluids is not suitable. This is an important part of the physics that has strong implications relevant for upscaling and modelling two-phase flows in microfluidic devices or highly permeable porous media.

1. Introduction

An accurate description of two-phase flows in high-permeability porous media is of major importance in several practical applications. This includes soil remediation in sandy or gravely soils [14], nuclear safety [9], or catalytic fixed bed reactors [33]. However, most of the literature on two-phase flows in porous media is focused on low-permeability porous media. For low-permeability porous media in the limit of creeping flows, surface tension forces often dominate the flow; thus the capillary, Bond, and Weber numbers are low. In that case, the fluid repartition is well described as two indepen-

dent flow paths for each phase [11, 6]. The two fluids are segregated, the non-wetting fluid flows into the larger pores, whereas the wetting fluid occupies the smaller pores. One of the consequences is that the area of the fluid-fluid interface is small (Fig. 1 (a)) and there is little drag between the fluid phases. In contrast, for high-permeability porous media, the flow is the result of a complex interaction between capillary, gravity, viscous, and inertial forces [10]. Capillary effects may no longer dominate and the capillary, Bond, and Weber numbers may be large. The distribution of fluids in the pore space can be schematically decomposed in two modes, even though the reality is often a lot more complex. Either
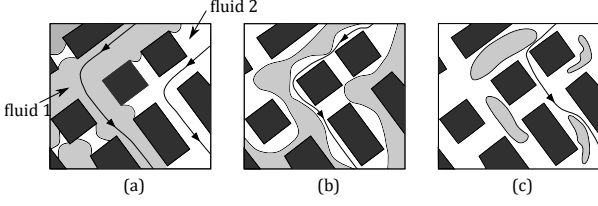
Figure 1: Schematics of possible distributions of fluids in a 2D porous network with solid phase in black, the non-wetting fluid (fluid 1) in light grey, and the wetting fluid (fluid 2) in white, (a) the two fluids are flowing in different channels separated by numerous meniscus and the fluid-fluid interface extent is small, (b) the wetting and non-wetting fluids are flowing together in most of the pores as two continuous streams and (c) both fluids are flowing together in most of the pores and the non-wetting phase is discontinuous. - Adapted from [11]

the non-wetting fluid is continuous and flows in the center of the pores surrounded by the wetting fluid flowing as a thin film in contact with the solid (Fig. 1 (b)), or the non-wetting fluid is discontinuous and flows in the center of the pores in the form of droplets or ganglias (Fig. 1 (c)). In both cases, the surface area between the fluids is large and the drag forces between the fluids are not negligible compared with the solid-fluids drag forces. This is in strong contrast with capillarity-dominated flow and it is important because, as discussed in the following, modelling of the drag forces is the basis of any attempt to establish continuous relationships on a macroscopic scale starting from the pore scale.

Models used to describe two-phase flows in porous media are often based on a direct extension of Darcy's equations for one-phase flow [38, 23]. This generalization depends on the introduction of relative permeabilities that essentially account for the division of the available void space between the fluids; thus each fluid phase acts as a supplementary solid regarding the other one and no interaction between the phases is taken into account [11, 6]. As a consequence, it is commonly assumed that the relative permeability only depends on the saturation [8, 35] and we know that this is not always accurate as relative permeabilities may also depend on the capillary number [20], the flow regime [2] or the viscosity ratio [40, 13, 39]. Since the early 1980s, numer-

ous works have aimed at improving the generalized Darcy equations on a sound physical basis. Using upscaling techniques, several authors proposed additional coupling terms that correspond to stresses at the fluid-fluid interface and yield coupling permeability tensors [22, 1, 36, 18]. The importance of these coupling terms in the overall flow process is not clear [3]. These additional terms can be calculated analytically in a two-phase annular cocurrent flow in a cylindrical capillary tube, and are of the same order as the dominant relative permeabilities [4]. However, other studies considered configurations for which the surface between fluids was smaller and concluded that coupling terms should not be as important [34, 27]. Zarcone and Lenormand [41], Dullien and Dong [12] and Ramakrishnan and Goode [28] directly measured the coupling permeability terms in natural media by performing steady-state cocurrent two-phase flows. Rose [30] proposed to indirectly measure the coupling relative permeability terms by performing two different types of experiments. This technique was also used for both cocurrent and countercurrent experiments [7, 5]. Each of these authors, except Zarcone and Lenormand, found that the coupling relative permeabilities are significant. Recently, Clavier et al. [9] performed experiments of inertial two-phase flows in coarse non-consolidated porous media and proposed constitutive models. However, results suffer from a major shortcoming. Indeed, it is impossible to know which type of flow regime dominates at the pore scale and thus the exact link between the physics at the pore-scale and the macroscale model.

Micromodels can be used to better understand two-phase flows in porous media [17], e.g. transitions between the flow regimes or the onset and development of displacement instabilities [19, 42]. Therefore, micromodels allow overcoming the major issue we have just risen. Such apparatus were employed to measure the relative coupling permeabilites for

2

different flow regimes [2] or study the impact of the fluid-fluid drag on the flow characteristics [15, 29]. Rothman [31] used numerical simulations in a 2D micromodel geometry and found that coupling permeabilities are comparable in magnitude with the case of the annular flow in a capillary tube. Fig. 2 shows Rothman's results along with some of the previously mentioned results on relative coupling permeabilities. Hele-Shaw cells are one of the simplest example of micromodels as they consist of two parallel plates in between which the fluids flow. Governing equations for the flow in such cells are similar to Darcy's equation, and thus the permeability can be easily modified by increasing or decreasing the aperture between the plates [32]. Recently, this characteristic has been used to investigate the flow paths of a two-phases flow as a function of the micromodel thickness [21] or to study the stability of an immiscible two-phases displacements in a Hele-Shaw cell with a spatially varying thickness [16]. Here, we study the influence of micromodel's absolute permeability on the fluid-fluid drag and solid-fluids drag for different capillary numbers. The original idea of the article is to solve the appropriate depth-averaged equations for two-phase flows in a Hele-Shaw cell to study the effect of the varying absolute permeability on the drag forces without having to change the in-plane geometry.

2. Pore-scale, depth-averaged and surface-averaged flow equations

In this section, we present the derivation of the averaged flow equations for two-phases flows in a Hele-Shaw cell, starting from the three-dimensional Stokes equations. Then, we average the momentum equations spatially to derive the unclosed form of the macroscopic momentum transport equations. The system under consideration is depicted in Fig. 3 which represents a quasi-planar cocurrent two-phase flow
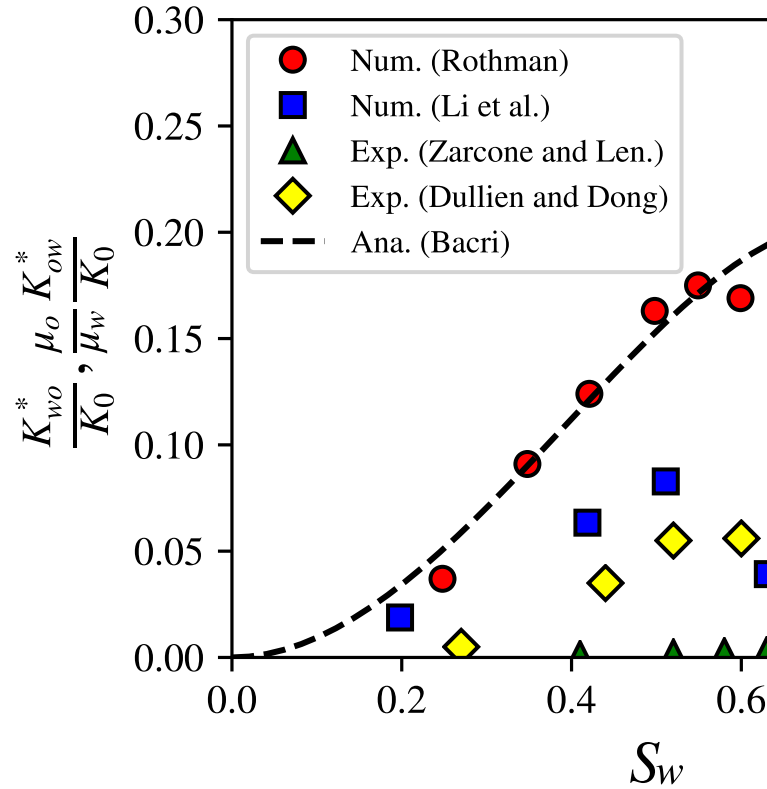

Figure 2: Normalized coupling relative permeabilities K_{ij}^* as a function of the wetting-fluid saturation S_w from experimental work [12, 41], numerical simulations [31, 20] and analytical solution for a steady-state annular two-phase flow in a circular capillary tube (dashed line) [4]. The capillary theoretical case provides an upper limit in terms of permeability and extent of the interfacial surface area between the fluids.
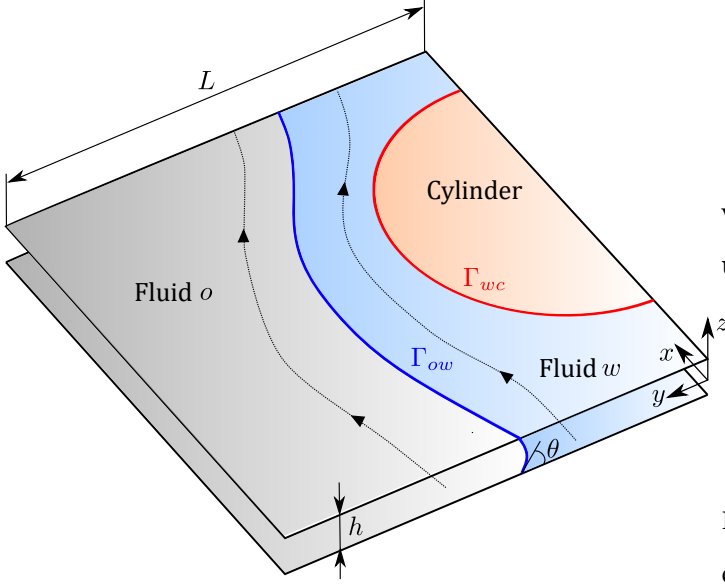
Figure 3: Schematic view of a cocurrent two-phase flow in a Hele-Shaw cell parallel to the $x - y$ plane with a wedge of circular cross-section as a solid obstacle. The transverse dimension of the cell is noted L and h stands for the aperture between the plates. The boundary between the wetting-fluid w and the cylinder (in red) is noted Γ_{wc} and the boundary between the two fluids (in blue) is noted Γ_{ow}. No dynamic films along the plates are considered here and θ stands for the non-zero contact angle between the two fluids and the plates.

between two parallel plates with a wedge of circular cross-section as a solid obstacle. The transverse dimension of the cell is noted L and h is the length of the aperture between the plates.

Pore-scale flow equations. Three-dimensional continuity and Stokes equations for a Newtonian fluid in the absence of external forcing read, respectively,

$$\nabla^* \cdot \mathbf{u} = 0, \qquad -\nabla^* p + \mu \nabla^{*2} \mathbf{u} = 0, \qquad (1)$$

where the superscript * indicates that the derivative operators are three-dimensional.

Depth-averaged flow equations. The starting point is to consider an aparatus such as depicted in Fig. 3 for which h is very small compared to the transverse length of the cell. It follows that the z-component of the velocity can be neglected and

$$\mathbf{u} = (u(x, y, z), v(x, y, z), 0)^T = f(z)\bar{\mathbf{u}}(x, y), \quad (2)$$

where we introduce the depth-averaged velocity defined as $\bar{\mathbf{u}} \equiv \frac{1}{h} \int_{-h/2}^{h/2} \mathbf{u} \, dz$. The in-plane version of Eq. 1 then read

$$\nabla \cdot \bar{\mathbf{u}} = 0, \qquad -\nabla p + \mu \left(\nabla^2 \bar{\mathbf{u}} + \bar{\mathbf{u}} \frac{\partial^2 f(z)}{\partial z^2} \right) = 0. \quad (3)$$

From the condition $\int_{-h/2}^{h/2} f(z) \, dz = h$, arising from the definition of the depth-averaged velocity, along with the no-slip boundary condition at $z \pm h/2$, we find that $f(z) = \frac{3}{2}(1 - 4\frac{z^2}{h^2})$. Then,

$$\nabla \cdot \bar{\mathbf{u}} = 0, \qquad \mu \left(\nabla^2 \bar{\mathbf{u}} - k^2 \bar{\mathbf{u}} \right) = \nabla p, \qquad (4)$$

are the continuity and momentum transport equations for the depth-averaged flow of one fluid and $k = \sqrt{12}/h$. It has been shown that the velocity profile for a flow in a rectangular channel with Eq. 4 lead to a reasonable approximation, up to aspect ratios $h/L = 1$, of the result obtained from the three-dimensional Stokes equations [24]. In the case of two-phase flows, these equations have to be written for each fluid and boundary conditions at the fluid-fluid interfaces are required. Continuity of the depth-averaged velocities across the interface and a jump of interface normal stress are sufficient if the surface tension is constant along the interface [26]. These conditions are expressed

$$\bar{\mathbf{u}}_o - \bar{\mathbf{u}}_w = 0 \text{ at } \Gamma_{ow}, \qquad (5)$$

$$(\bar{\sigma}_w - \bar{\sigma}_o) \cdot \mathbf{n}_{ow} = \gamma \left(\frac{\pi}{4} \kappa_{\parallel} + \frac{2}{h} \cos\theta \right) \mathbf{n}_{ow} \text{ at } \Gamma_{ow}, \quad (6)$$

4

where $\bar{\sigma}_i$ is the in-plane stress tensor of fluid i, $\mathbf{n}_{ow}$ is the in-plane normal vector at the fluid interface pointing toward the fluid w, γ is the surface tension, $\kappa_\parallel$ is the in-plane interface curvature and θ denotes the contact angle between the fluid interface and the plates (Fig. 3). The meniscus in the z-direction is approximated as a half-circle of radius $h/2$ and the $\pi/4$ correction for the in-plane curvature was derived by Park and Homsy [26]. In Eq. 6, we neglected the additional terms that pertain to the formation of the dynamic film [26] which scaled non-linearly with the capillary number. We rather considered a non-zero contact angle, and consequently, the absence of such thin films.

Volume-averaged flow equations. Here, we proceed to the spatial averaging of the in-plane momentum transport equations. We recall that all the flow variables and differential operators have components only in the transverse direction. According to the volume averaging framework [37] and acknowledging that Eq. 4 are two-dimensional, the traditional averaging theorem for the depth-averaged quantity $\bar{\omega}_i$ associated with the fluid i reads

$$\langle \nabla \bar{\omega}_i \rangle = \nabla \langle \bar{\omega}_i \rangle + \frac{1}{S} \int_{\Gamma_{ic}} \mathbf{n}_{ic} \bar{\omega}_i \, \mathrm{d}\Gamma + \frac{1}{S} \int_{\Gamma_{ij}} \mathbf{n}_{ij} \bar{\omega}_i \, \mathrm{d}\Gamma, \quad (7)$$

where,

$$\langle \bar{\omega}_i \rangle = \frac{1}{S} \int_{S_i} \bar{\omega}_i \, \mathrm{d}S, \tag{8}$$

is the superficial surface average and S is the surface of a representative elementary cell. Applying the superficial surface average of Eq. 4 along with the averaging theorem and using traditional length-scale arguments [37] we obtain

$$\nabla \cdot \langle \bar{\mathbf{u}}_i \rangle = 0, \quad i, j = o, w, \ i \neq j, \tag{9a}$$

$$\frac{1}{S} \int_{\Gamma_{ic}} \mathbf{n}_{ic} \cdot \left(-p_i \mathbf{I} + \mu_i \left(\nabla \bar{\mathbf{u}}_i + (\nabla \bar{\mathbf{u}}_i)^T \right) \right) \, \mathrm{d}\Gamma +$$
$$+ \frac{1}{S} \int_{\Gamma_{ij}} \mathbf{n}_{ij} \cdot \left(-p_i \mathbf{I} + \mu_i \left(\nabla \bar{\mathbf{u}}_i + (\nabla \bar{\mathbf{u}}_i)^T \right) \right) \, \mathrm{d}\Gamma -$$
$$- \mu_i k^2 \langle \bar{\mathbf{u}}_i \rangle = \varepsilon_i \nabla \langle p_i \rangle^i + \langle p_i \rangle^i \nabla \varepsilon_i, \quad i, j = o, w, \ i \neq j, \tag{9b}$$

where $\mathbf{I}$ is the 2×2 identity matrix and $\langle p_i \rangle^i$ $\left(\langle p_i \rangle^i = \langle p_i \rangle / \varepsilon_i \right)$ is the intrinsic surface average pressure of fluid i, with ε_i the volume fraction of fluid i. The first integral is the drag force exerted upon the cylinders boundary by fluid i and the second integral pertains for the drag force exerted upon fluid j by fluid i. Here, we consider that the contour of the fluid-fluid interface in the $x - y$ plane can be identically translated along the z-direction, which is an approximation since the meniscus is a half-circle for small h/L ratio. However, as shown in the Appendix Appendix A, using three-dimensional flow simulations in microchannels, these approximations remain reasonable.

If the variation of the saturation in space is negligible and acknowledging that, as illustrated in Fig. 3, only the wetting fluid w is in contact with the wedge, a more compact form of Eq. 9b reads

$$0 = -\varepsilon_w \nabla \langle p_w \rangle^w - \mu_w k^2 \langle \bar{\mathbf{u}}_w \rangle + \mathbf{d}_{wc} + \mathbf{d}_{wo}, \tag{10a}$$

$$0 = -\varepsilon_o \nabla \langle p_o \rangle^o - \mu_o k^2 \langle \bar{\mathbf{u}}_o \rangle + \mathbf{d}_{ow}, \tag{10b}$$

Here, $\mathbf{d}_{ij}$ $\left(\mathbf{d}_{ij} = \int_{\Gamma_{ij}} \sigma_i \cdot \mathbf{n}_{ij} \, \mathrm{d}\Gamma \right)$ denotes the drag forces per unit surface area exerted upon phase j by phase i and which must be computed or modeled to obtain closed macroscopic equations. In the following, we are working on the direct calculation of each drag force terms summarized in Tab. 1.

Drag of upon	Fluid o	Fluid w	
Plates	$-\mu_o\langle\bar{\mathbf{u}}_o\rangle\frac{12}{h^2}$	$-\mu_w\langle\bar{\mathbf{u}}_w\rangle\frac{12}{h^2}$	$\Sigma = \mathbf{d}_s$
Wedge	-	$\mathbf{d}_{wc}$	
Fluid o	-	$\mathbf{d}_{wo}$	$\Sigma = \mathbf{d}_f$
Fluid w	$\mathbf{d}_{ow}$	-	

Table 1: Summary of each drag force terms involved in the averaged momentum transport equation for two-phase flow in a Hele-Shaw cell.

3. Direct numerical simulations

In this section, we introduce the standard Level Set method to capture the moving free interface between the fluids, along with the flow equations, both solved with a Finite Element solver.

3.1. Equations

Level Set model. The Level Set method is an Eulerian method that easily handles the topological phases changes, in contrast with Lagrangian methods. Here, the fluid phases are identified with a phase color function that goes smoothly from 0 to 1 across the fluid interface with the manifold defined as the iso-level $\phi = 0.5$. Transport of the level set function ϕ is governed by

$$\frac{\partial \phi}{\partial t} + \nabla \cdot (\bar{\mathbf{u}}\phi) = \tau \nabla \cdot \left(\psi \nabla \phi - \phi(1-\phi)\frac{\nabla \phi}{|\nabla \phi|} \right), \quad (11)$$

where $\bar{\mathbf{u}}$ is the depth-averaged velocity field and τ and ψ are two numerical parameters that control the diffuse interface thickness and the amount of initialization of ϕ function, respectively [25]. We investigated the accuracy of the implicit definition of the interface as well as the effect of the value of the initialization parameter on the interface position in Appendix Appendix B by comparing to a boundary element method Nagel and Gallaire [24].

The governing flow equations read

$$0 = \nabla \cdot \bar{\mathbf{u}} \quad (12a)$$

$$0 = -\nabla p + \mu(\phi)\left(\nabla^2\bar{\mathbf{u}} - \frac{12}{h^2}\bar{\mathbf{u}}\right) + \gamma\left(\frac{\pi}{4}\nabla \cdot \left(\frac{\nabla \phi}{|\nabla \phi|}\right) - \frac{2}{h}\right)\delta(\phi)\mathbf{n}, \quad (12b)$$

where δ is the Dirac delta function localized on the interface and $\mathbf{n}$ denotes the unit normal to the interface, respectively defined as,

$$\delta(\phi) = 6\,|\nabla \phi|\,|\phi(1+\phi)|, \quad \text{and} \quad \mathbf{n} = \frac{\nabla \phi}{|\nabla \phi|}. \quad (13)$$

We introduce the following reference and dimensionless quantities,

$$\bar{\mathbf{u}} = \bar{\mathbf{u}}' \times U_r, \ p = p' \times \frac{\mu_r U_r}{L}, \ \mathbf{x} = \mathbf{x}' \times L, \quad (14)$$

and the dimensionless continuity and momentum transport equations are

$$0 = \nabla' \cdot \bar{\mathbf{u}}' \quad (15a)$$

$$0 = -\nabla'p' + \frac{\mu(\phi)}{\mu_r}\left(\nabla'^2\bar{\mathbf{u}}' - \frac{12}{(h/L)^2}\bar{\mathbf{u}}'\right) + \frac{\gamma}{\mu_r U_r}\left(\frac{\pi}{4}\nabla' \cdot \left(\frac{\nabla'\phi}{|\nabla'\phi|}\right)\right) \quad (15b)$$

with $\delta'(\phi) = 6\,|\nabla'\phi|\,|\phi(1+\phi)|$. We therefore have three dimensionless numbers: the viscosity ratio $M(\phi) = \frac{\mu(\phi)}{\mu_r}$, the capillary number $Ca^{-1} = \frac{\gamma}{\mu_r U_r}$ and the aspect ratio $h^* = h/L$.

Geometry, boundary conditions and simulation parameters. Our macroscopic model is a Hele-Shaw cell with wedges of cylindrical cross-section. This system is subdivided into seven unit-cell (UC) subdomains encompassing one wedge, as depicted in Fig. 4. Taking advantage of the symmetry, we stud-

Symmetry

UC1 UC2 UC3 UC4 UC5 UC6 UC7

Inlet o

Inlet w

Symmetry

no-flow

y

x

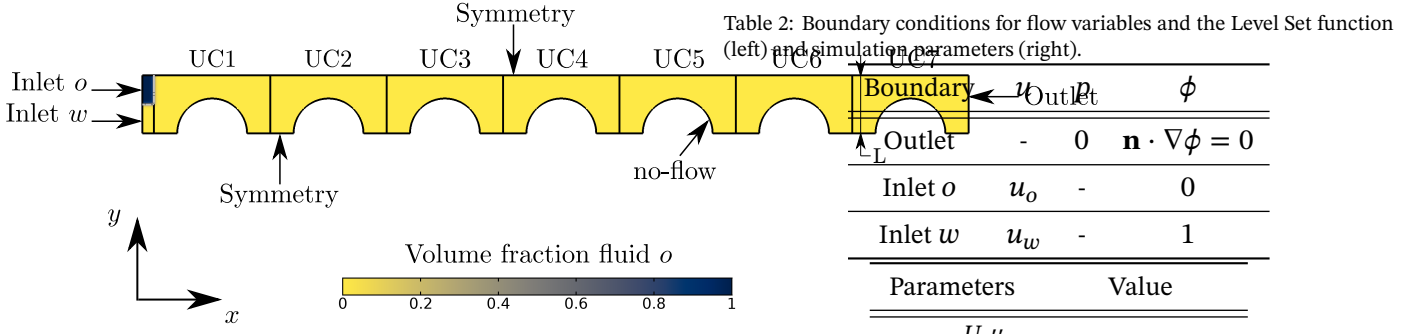Volume fraction fluid o

0   0.2   0.4   0.6   0.8   1

Figure 4: Schematics of the geometry and initial condition. We consider the superior half of an array of five cylindrical wedges inside five cuboids where both fluids are injected from left to right. Initially, the model is saturated with wetting fluid (red), and the width L of one Unit Cell (UC) is 5×10^{-4} m. Symmetry boundary conditions are used on both length sides and the no-flow boundary condition is imposed at the wedge boundary.

Table 2: Boundary conditions for flow variables and the Level Set function (left) and simulation parameters (right).

Boundary	u	p	ϕ
Outlet	-	0	$\mathbf{n} \cdot \nabla \phi = 0$
Inlet o	u_o	-	0
Inlet w	u_w	-	1

Parameters	Value
$Ca = \dfrac{U_t \mu_o}{\gamma}$	from 0.5 to 0.02
$M_w = \dfrac{\mu_w}{\mu_o}$	1
$f_f = \dfrac{u_w}{U_t}$	1/4
$h^* = h/L$	from 5 to 1/20

ied only the upper half of a row. Each fluid flows from left to right (x-direction) and the inlet boundary conditions for both fluids are a constant normal inlet velocity u_i. The outlet boundary condition for the flow is a reference pressure. The boundary conditions used are summarized in Tab.2. We choose the total inlet velocity as the reference velocity; thus the dimensionless inlet velocities can be expressed as a fractional flow f_f,

$$f_f = \frac{u_w}{U_t}, \quad u_o = 1 - f_f, \quad \text{with} \quad U_t = u_w + u_o. \quad (16)$$

The non-wetting viscosity is taken as the reference viscosity and the respective value of each dimensionless parameters is in Tab. 2. The initialization parameter value is equal to the maximum inlet velocity value, which yields maximum accuracy (Appendix Appendix B). As a reference, we conducted numerical simulations of one-phase flows and found that the range of aperture corresponds to a range absolute permeabilities between 1.5×10^4 and 40 darcy.

Mesh convergence study. Here, we study the mesh convergence of the various drag forces. The dimensionless numbers for this study are $Ca = 0.5$, $h^* = 1/4$, $f_f = 0.25$ and $M = 1$. In Fig. 5 (a) the results are normalized with respect to the finer mesh result and are given as a function of the total number of degree of freedom in the whole model. The fluid-fluid interface position for three different mesh densities is given in Fig. 5 (b). We obtain these results in the fourth unit-cell (UC4) at steady-state. The drag terms are not very sensitive to the mesh density and the interface between the fluids is correct even for a coarse mesh and converges quickly. In the following simulations, we use a mesh that corresponds to 3.7×10^5 degree of freedoms
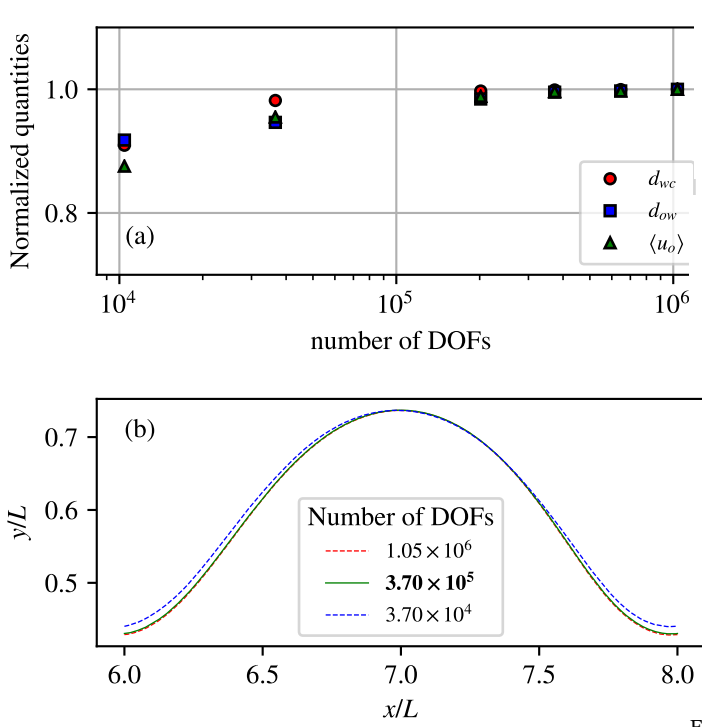
Figure 5: Mesh convergence study of (a) drag force exerted upon the wedge (red), drag force exerted upon the fluid-fluid boundary (blue) and intrinsic average velocity of fluid o (green). All the results are normalized with respect to the result obtained with the finer mesh, at steady-state and in UC4. (b) Fluid-fluid interface position in UC4 at steady-state for different number of degree of freedoms in the whole geometry. Flow parameters are $Ca = 0.5$, $h^* = 1/4$, $f_f = 0.25$ and $M = 1$. In the following we use a mesh that corresponds to 3.7×10^5 degree of freedoms.
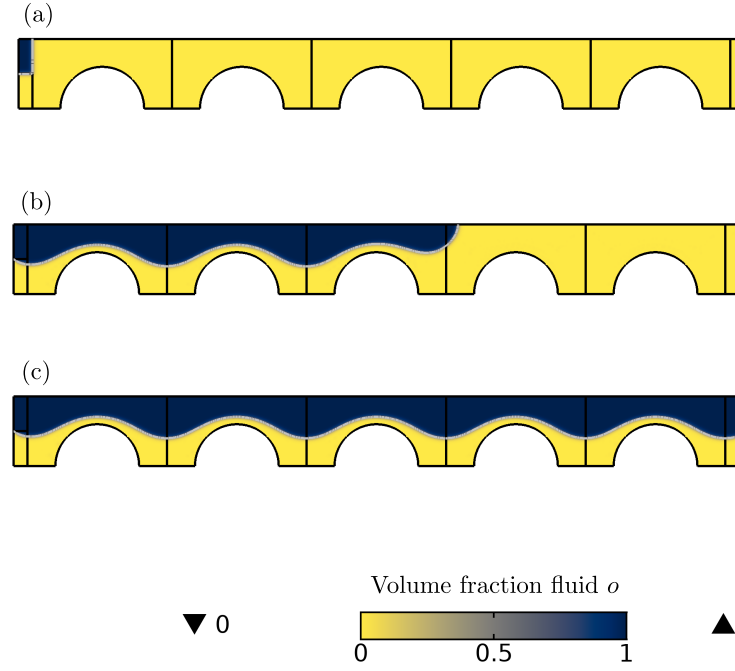
Figure 6: Fluids repartition along the superior half-row at (a) the initial time, (b) for an intermediate time and (c) final time (steady-state reached) for $Ca = 0.1$, $f_f = 0.25$, $M = 1$ and $h^* = 1/8$. At steady-state the fluid-fluid interface taken on the central unit cells is periodic whereas it is slightly deformed in the first and last UC under the influence of the boundary conditions.

4. Results and discussion

Before presenting the results for drag force terms, we briefly discuss the two-phase flow regime observed along with the variation of the saturation with time. The flow regime is fundamental as it drives the extent of the interfacial surface area between the fluids.

Two-phase flow regimes. We observe that the two fluids remain continuous at all times and for the entire range of tested capillary numbers and aperture. The interface between the fluids becomes stationary and a stationary state is reached for every capillary number and aperture values. Fig. 6 shows the initial, intermediate, and final configurations of the fluid repartition for the case $Ca = 1 \times 10^{-1}$ and $h^* = 1/8$. At

steady-state, the fluid-fluid interface is periodic on the five central unit cells whereas the interface is slightly deformed at the inlet and outlet cells, under the influence of boundary conditions.

We could have expected a break-up of the invading phase either by snap off phenomena, or by the shear action of the wetting fluid flow. However, the pore throat is large and the fractional flow is low, which favours the continuity of the fluid phases. The flow regime observed is therefore a film-flow regime within the limit of the parameters chosen for this study. We obtained all the following results in the fourth unit-cell (UC4) in order to be far from the influence of the inlet and outlet boundary conditions.

Saturation. Wetting fluid saturation at steady-state decreases, in average, from 0.6 to 0.4 as the aperture between the plates decreases from 5 to 1/20. This can be seen in Fig. 7, which

8

Figure 8: Comparison of interface position for different aperture (a) $Ca = 5 \times 10^{-1}$ and (b) $Ca = 2 \times 10^{-2}$ (in UC4 for $f_f = 0.25$ and $M = 1$).
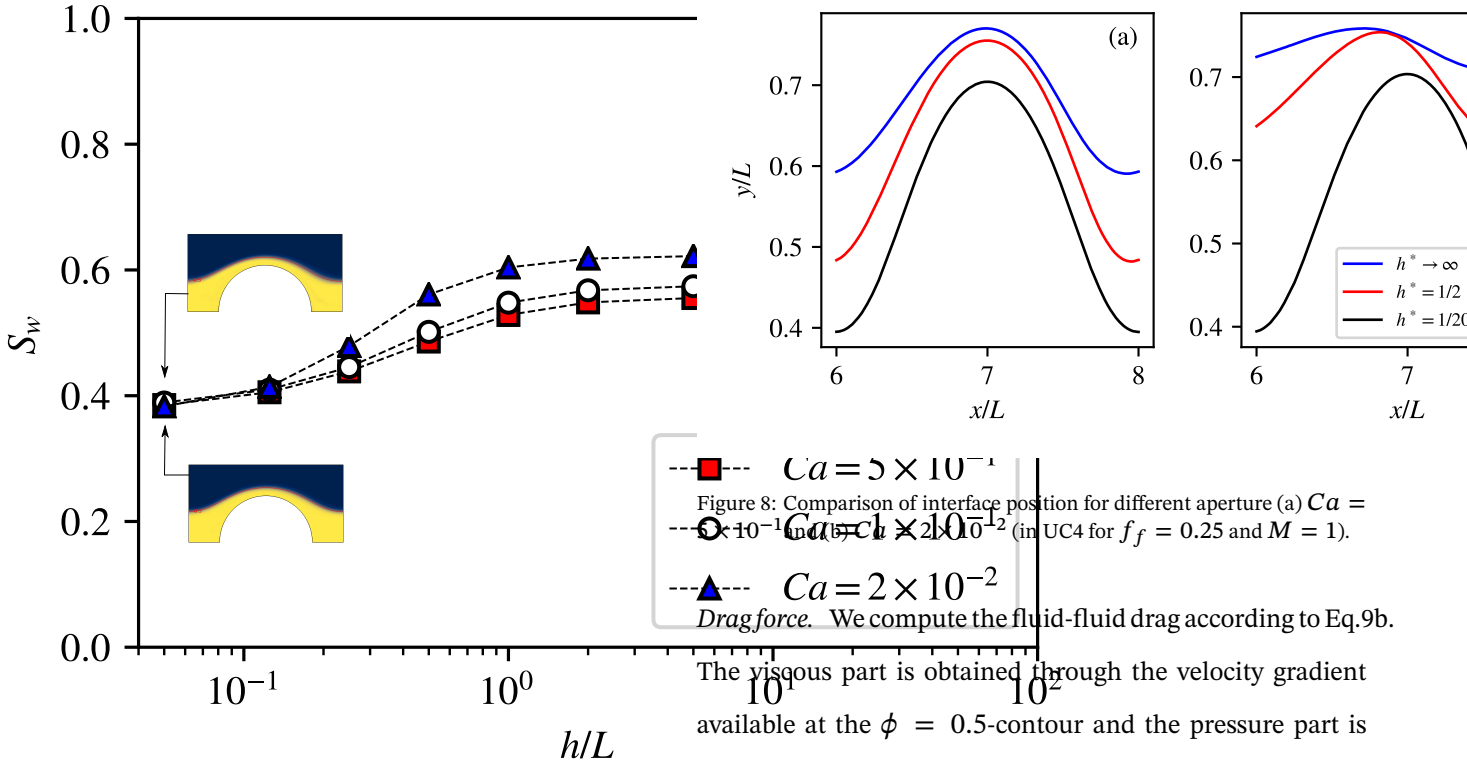
Figure 7: Fluid saturation at steady-state in UC4 as a function of the dimensionless aperture and for different capillary numbers. Fields of the level-set function at steady-state in UC4 are given for the selected value of the dimensionless aperture and $Ca = 5 \times 10^{-1}$ and $Ca = 2 \times 10^{-2}$. As the aperture increases the interface flattens and the wetting fluid saturation increases. A decrease in the capillary number acts in the same way, albeit less strongly. The 2D limit case is given with plain black markers.

presents the saturation in UC4 as a function of the dimensionless aperture and for different capillary numbers. The saturation does not depend on the capillary number for the smallest apertures. However, as the aperture between the plates increases, the fluid-fluid interface becomes flatter and the saturation of the wetting fluid increases until it converges to the saturation obtained for the 2D limit case which values slightly depend on the capillary number (see saturation fields insets in Fig. 7). Fig. 8 compares the position of the fluid-fluid interface in UC4 for different aperture and capillary numbers. For $Ca = 5 \times 10^{-1}$ the interface is symmetric regardless the aperture's value, whereas the interface is non-symmetric for low Ca and small aperture.

Drag force. We compute the fluid-fluid drag according to Eq. 9b. The viscous part is obtained through the velocity gradient available at the $\phi = 0.5$-contour and the pressure part is obtained by application of the divergence theorem. In the following, we are interested in the drag force component in the x-direction, i.e., the main flow direction. The drag force exerted upon the solid-fluids boundaries, denoted d_s^x, is the sum of the drag upon the wedge and upon the cell plates by both fluids, as defined in Tab 1. The fluid-fluid drag, denoted d_f^x, is the sum $d_f^x = d_{ow}^x + d_{wo}^x$. In the following, the x–component of the drag forces are expressed per unit surface area of unit-cell.

Fig. 9 shows the ratio of the fluid-fluid drag over the solid-fluid drag as a function of the aperture between the plates and different values of capillary number. Our results show that the fluid-fluid drag is non-negligible compared to the solid-fluid drag. At most, the fluid-fluid drag reaches 80% of the value of the solid-fluid drag and this occur for high Ca and large aperture. The results from the purely 2d simulations ($h^* \to \infty$) indicate that for $h/L = 5$, the larger aperture tested, the contribution of the drag upon the plates is already insignificant. Then, by narrowing the aperture, the
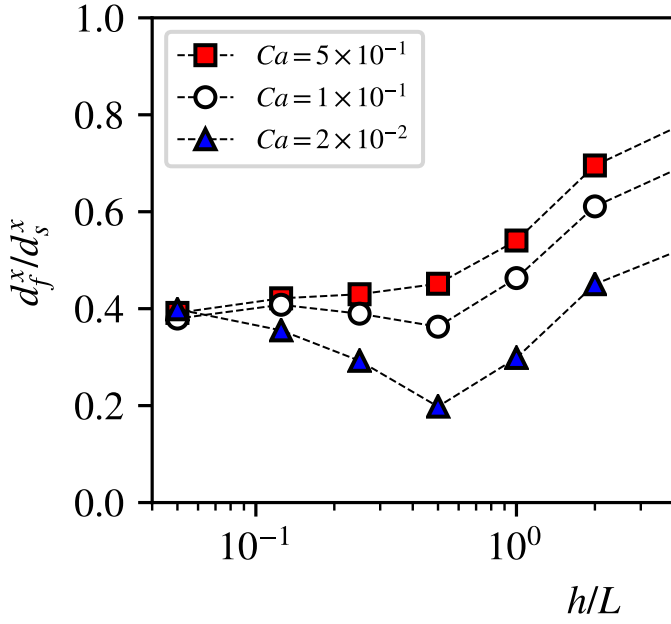
9

Figure 9: Ratio of fluid-fluid drag force over solid-fluid drag force as a function of the dimensionless aperture and for different capillary numbers (in UC4 for $f_f = 0.25$ and $M = 1$). The 2D limit case is given with plain black markers.
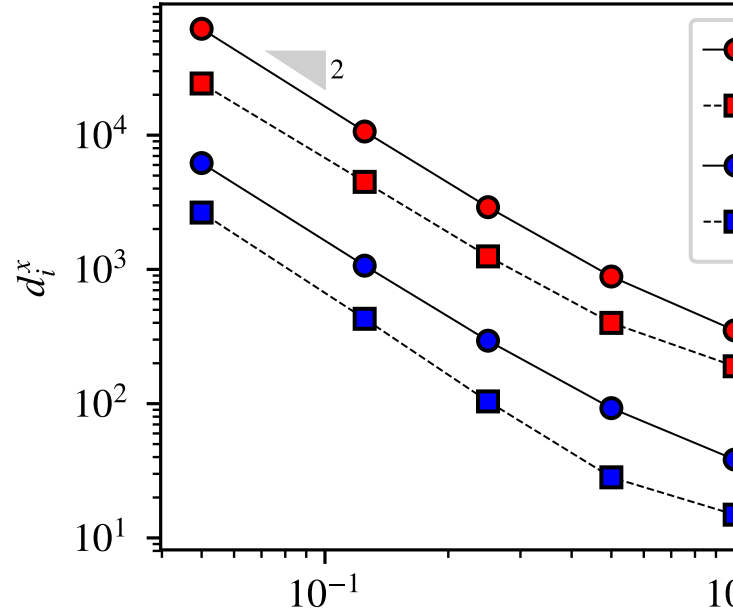

Figure 10: Comparison of fluid-fluid and solid-fluid drag force as a function of the dimensionless aperture for two capillary numbers (in UC4 for $f_f = 0.25$ and $M = 1$).

fluid-fluid drag decreases compared to the solid-fluid drag, until $h^* = 1/2$. From $h^* = 1/2$ and below the fluid-fluid drag either remains constant, for the higher Ca, or increases. In the end, for the smallest aperture, the importance of the fluid-fluid drag does not depend on the capillary number and is 40% of the value of the solid-fluid drag.

Regarding the limit case of infinite aperture the capillary number is important

Fig. 10 shows the fluid-fluid ant the solid-fluid drag forces as a function of the aperture and for two capillary numbers. Here again, the dimensionless aperture $h^* = 1/2$ signal a change in the drag behavior. For $1/2 < h^*$, the fluid-fluid and solid-fluid drag forces barely change with the aperture whereas, for $h^* < 1/2$ both drag forces scale approximately as h^{-2}.

Fig. 11 shows the proportion of the solid-fluid drag which is due to the drag exerted upon the wedge as a function of

the aperture. Here the 2D limit case is clear since the solid-fluid drag is only due to the drag upon the wedge in that case. The importance of the drag upon the wedge decreases as the aperture decrease, however it remains non-negligible (40% of the solid-fluid drag) even for the smallest aperture $h^* = 1/20$.

Fig. 12 shows the proportion of the fluid-fluid and solid-fluid drag upon the wedge which is due to the pressure part of the stress-tensor. The pressure part produces most of the drag force, either regarding the fluid-fluid or the solid-fluid drag upon the wedge, for $h^* < 1/2$. For larger aperture, the fluid-fluid drag is mainly produced by the viscous part, whereas the pressure part has a minimum contribution as high as 60% of d_{wc}.
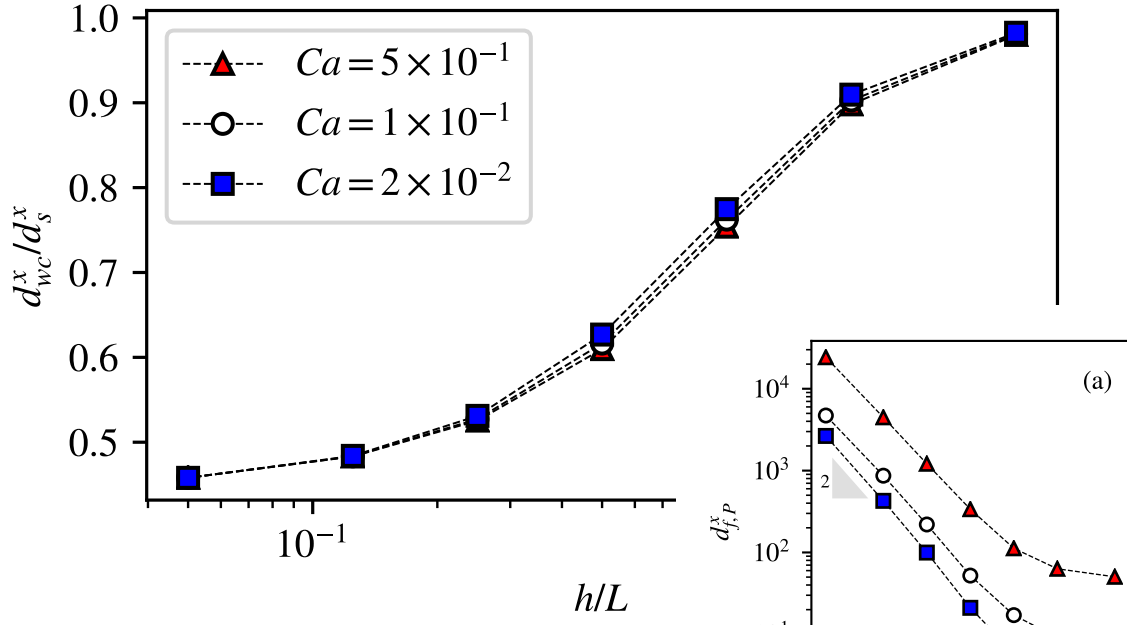
Figure 11: Proportion of the solid-fluid drag force due to the contribution of the drag exerted upon the wedge, as a function of the dimensionless aperture and for different capillary numbers (in UC4 for $f_f = 0.25$ and $M = 1$).
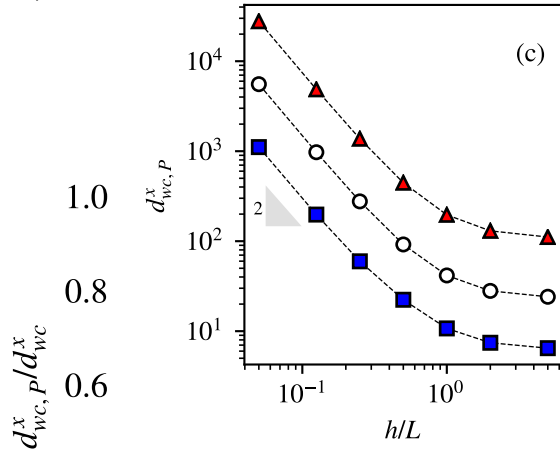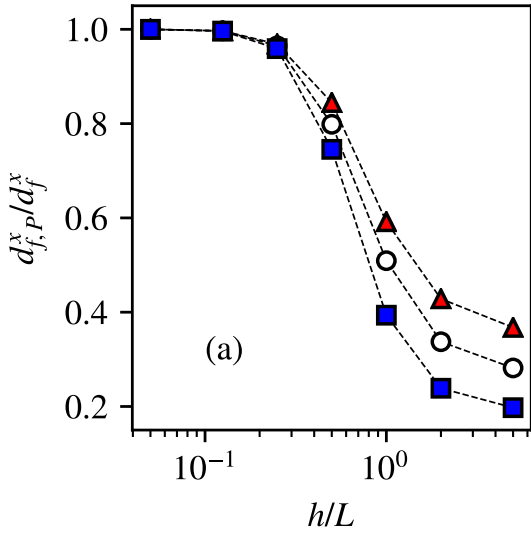

Figure 12: Proportion of the fluid/fluid drag (a) or the solid-fluid drag upon the wedge (b) due to the pressure term contribution, as a function of the dimensionless aperture and for different capillary numbers (in UC4 for $f_f = 0.25$ and $M = 1$)
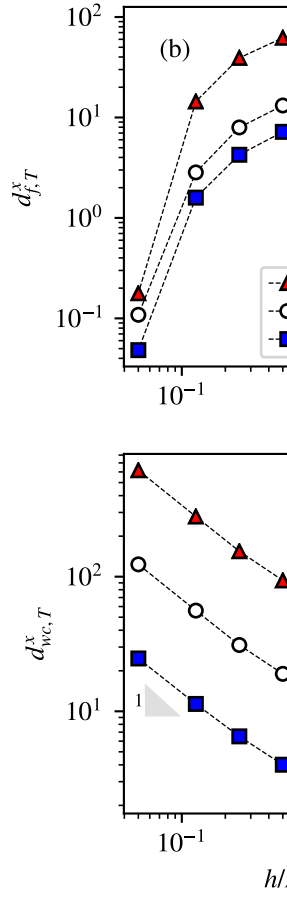

Figure 13: Comparison of the drag produced by the pressure for

5. Conclusion

In this study we conducted direct simulations of depth-averaged two-phases flows, and we investigated the effect of the permeability on the drag forces exerted upon the different phase interfaces. The permeability was changed by varying the Darcean term which arising from the depth-averaging, thus without altering the in-plane geometry. These drag terms have to be modelled to obtain the macroscopic momentum transport equations but the drag exerted upon the the fluid-fluid interface is commonly neglected for flow driven by capillarity forces. Here we focused on film-flow regime pourencountered in two-phases flows in high permeability porous media or in microfluidic devices. We found that the drag exerted upon the fluid-fluid interface should not be neglected into the momentum transport equations for film-flow regimes. Lower permeability does not make the drag force terms at the interface negligible as long as the flow regime remains a film regime. On the contrary, the fluid-fluid drag force increases faster than the drag upon the fluid-solid interfaces, as the aperture between the plates decreases.

References

[1] Auriault, J., Sanchez-Palencia, E., 1986. Remarques sur la loi de darcy pour les écoulements biphasiques en milieu poreux. Journal of Theoretical and Applied Mechanics, Numéro Spécial , p141–156.

[2] Avraam, D.G., Payatakes, A.C., 1995. Generalized relative permeability coefficients during steady-state two-phase flow in porous media, and correlation with the flow mechanisms. Transport in Porous Media 20, 135–168. doi:10.1007/bf00616928.

[3] Ayub, M., Bentsen, R.G., 1999. Interfacial viscous coupling: a myth or reality? Journal of Petroleum Science and Engineering 23, 13–26.

[4] Bacri, J.C., Chaouche, M., Salin, D., 1990. Modèle simple de perméabilités relatives croisées. Comptes rendus de l'Académie des sciences. Série 2, Mécanique, Physique, Chimie, Sciences de l'univers, Sciences de la Terre 311, 591–597.

[5] Bentsen, R.G., Manai, A.A., 1993. On the use of conventional cocurrent and countercurrent effective permeabilities to estimate the four generalized permeability coefficients which arise in coupled, two-phase flow. Transport in Porous Media 11, 243–262.

[6] Blunt, M.J., 2017. Multiphase flow in permeable media: A pore-scale perspective. Cambridge University Press.

[7] Bourbiaux, B.J., Kalaydjian, F.J., et al., 1990. Experimental study of cocurrent and countercurrent flows in natural porous media. SPE Reservoir Engineering 5, 361–368.

[8] Brooks, R., Corey, T., 1964. Hydrau uc properties of porous media. Hydrology Papers, Colorado State University 24, 37.

[9] Clavier, R., Chikhi, N., Fichot, F., Quintard, M., 2017. Modeling of inertial multi-phase flows through high permeability porous media: Friction closure laws. International Journal of Multiphase Flow 91, 243–261.

[10] Davit, Y., Quintard, M., 2018. One-phase and two-phase flow in highly permeable porous media. Heat Transfer Engineering , 1–19.

[11] Dullien, F.A.L., 2012. Porous media: fluid transport and pore structure. Academic press.

[12] Dullien, F.A.L., Dong, M., 1996. Experimental determination of the flow transport coefficients in the coupled equations of two-phase flow in porous media. Transport in Porous Media 25, 97–120. doi:10.1007/bf00141264.

[13] Ehrlich, R., 1993. Viscous coupling in two-phase flow in porous media and its effect on relative permeabilities@bookbear2013dynamics, title=Dynamics of fluids in porous media, author=Bear, Jacob, year=2013, publisher=Courier Corporation . Transport in Porous Media 11, 201–218.

[14] Fetter, C.W., Boving, T., Kreamer, D., 2017. Contaminant hydrogeology. Waveland Press.

[15] Heshmati, M., Piri, M., 2018. Interfacial boundary conditions and residual trapping: A pore-scale investigation of the effects of wetting phase flow rate and viscosity using micro-particle image velocimetry. Fuel 224, 560 – 578. URL: `http://www.sciencedirect.com/science/article/pii/S0016236118303971`, doi:`https://doi.org/10.1016/j.fuel.2018.03.010`.

[16] Jackson, S., Power, H., Giddings, D., Stevens, D., 2017. The stability of immiscible viscous fingering in hele-shaw cells with spatially varying permeability. Computer Methods in Applied Mechanics and Engineering 320, 606–632.

[17] Karadimitriou, N., Hassanizadeh, S., 2012. A review of micromodels and their use in two-phase flow studies. Vadose Zone Journal 11.

[18] Lasseux, D., Quintard, M., Whitaker, S., 1996. Determination of permeability tensors for two-phase flow in homogeneous porous media: theory. Transport in Porous Media 24, 107–137.

[19] Lenormand, R., Touboul, E., Zarcone, C., 1988. Numerical models and experiments on immiscible displacements in porous media. Journal of fluid mechanics 189, 165–187.

[20] Li, H., Pan, C., Miller, C.T., 2005. Pore-scale investigation of viscous coupling effects for two-phase flow in porous media. Physical Review E 72. doi:`10.1103/physreve.72.026705`.

[21] Liu, J., Ju, Y., Zhang, Y., Gong, W., 2019. preferential paths of air-water two-phase flow in porous structures with special consideration of channel thickness effects. Scientific reports 9, 1–13.

[22] Marle, C.M., 1982. On macroscopic equations governing multiphase flow with diffusion and chemical reactions in porous media. International Journal of Engineering Science 20, 643 – 662. doi:`https://doi.org/10.1016/0020-7225(82)90118-5`.

[23] Muskat, M., 1938. The flow of homogeneous fluids through porous media. Soil Science 46, 169.

[24] Nagel, M., Gallaire, F., 2015. Boundary elements method for microfluidic two-phase flows in shallow channels. Computers & Fluids 107, 272–284.

[25] Olsson, E., Kreiss, G., Zahedi, S., 2007. A conservative level set method for two phase flow ii. Journal of Computational Physics 225, 785 – 807. doi:`https://doi.org/10.1016/j.jcp.2006.12.027`.

[26] Park, C.W., Homsy, G., 1984. Two-phase displacement in hele shaw cells: theory. Journal of Fluid Mechanics 139, 291–308.

[27] Rakotomalala, N., Salin, D., Yortsos, Y.C., 1995. Viscous coupling in a model porous medium geometry: Effect of fluid contact area. Applied scientific research 55, 155–169.

[28] Ramakrishnan, T.S., Goode, P.A., 2015. Measurement of off-diagonal transport coefficients in two-phase flow in porous media. Journal of colloid and interface science 449, 392–398.

[29] Roman, S., Soulaine, C., Kovscek., A.R., 2019. Pore-scale visualization and characterization of viscous dissipation in porous media. Journal of Colloid and Interface Science doi:`https://doi.org/10.1016/j.jcis.2019.09.072`.

[30] Rose, W., 1988. Measuring transport coefficients necessary for the description of coupled two-phase flow of immiscible fluids in porous media. Transport in Porous Media 3, 163–171. URL: `https://doi.org/10.1007/BF00820343`, doi:`10.1007/BF00820343`.

[31] Rothman, D.H., 1990. Macroscopic laws for immiscible two-phase flow in porous media: Results from numerical experiments. Journal of Geophysical Research 95, 8663. doi:`10.1029/jb095ib06p08663`.

[32] Saffman, P.G., Taylor, G.I., 1958. The penetration of a fluid into a porous medium or hele-shaw cell containing a more viscous liquid. Proceedings of the Royal Society of London. Series A. Mathematical and Physical Sciences 245, 312–329.

[33] de Santos, J.M., Melli, T.R., Scriven, L.E., 1991. Mechanics of gas-liquid flow in packed-bed contactors. Annual Review of Fluid Mechanics 23, 233–260. doi:`10.1146/annurev.fl.23.010191.001313`.

[34] Scott, P., Rose, W., et al., 1953. An explanation of the yuster effect. Journal of Petroleum Technology 5, 19–20.

[35] Van Genuchten, M.T., 1980. A closed-form equation for predicting the hydraulic conductivity of unsaturated soils 1. Soil science society of America journal 44, 892–898.

[36] Whitaker, S., 1986. Flow in porous media II: The governing equations for immiscible, two-phase flow. Transport in porous media 1, 105–125.

[37] Whitaker, S., 2013. The method of volume averaging. volume 13. Springer Science & Business Media.

[38] Wyckoff, R.D., Botset, H.G., 1936. The flow of gas-liquid mixtures through unconsolidated sands. Physics 7, 325–345.

[39] Yiotis, A.G., Psihogios, J., Kainourgiakis, M.E., Papaioannou, A., Stubos, A.K., 2007. A lattice boltzmann study of viscous coupling effects in immiscible two-phase flow in porous media. Colloids and Surfaces A: Physicochemical and Engineering Aspects 300, 35 – 49. doi:`https://doi.org/10.1016/j.colsurfa.2006.12.045`. proceedings of the Fourth International TRI/Princeton Workshop.

[40] Yuster, S., et al., 1951. Theoretical considerations of multiphase flow in idealized capillary systems, in: Proceedings of the Third World Petroleum Congress, E. Brill The Hague. pp. 437–445.

[41] Zarcone, C., Lenormand, R., 1994. Détermination expérimentale du couplage visqueux dans les écoulements diphasiques en milieu

poreux. Comptes rendus de l'Académie des sciences. Série II, Mécanique, physique, chimie, astronomie 318, 1429–1435.

[42] Zhang, C., Oostrom, M., Wietsma, T.W., Grate, J.W., Warner, M.G., 2011. Influence of viscous and capillary forces on immiscible fluid displacement: Pore-scale experimental study in a water-wet micromodel demonstrating viscous and capillary fingering. Energy & Fuels 25, 3493–3505.
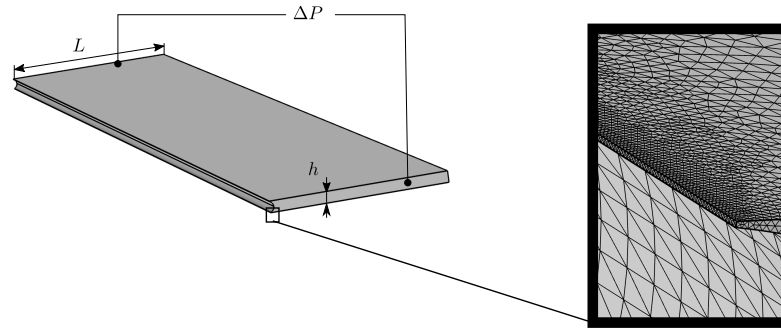
Figure A.14: Microchannel with one side is a half-circle wall and the opposite side is a flat wall with $h/L = 1/16$ (left) and mesh detail at the small chamfer build after the cylinder extrusion (right).

Appendix A. Approximation made on the drag force when considering a fluid-fluid flat interface

We conduct three-dimensional one-phase flow simulations into a microchannel to determine the approximation made on the drag calculation when considering that the fluid-fluid contour can be translated along the z-direction.

One side of the microchannel is a half-circle wall to mimic a fluid-fluid interface whereas the opposite side is a flat wall (Fig. A.14). We obtain the curved side by extruding a cylinder; thus a special treatment is done to correctly meshed the very thin part left, and we build very small chamfers (Fig. A.14). We compute the drag force per unit surface area on each side-wall of the microchannel and plot in Fig. A.15 the drag force exerted upon the curved side normalized with respect to the flat wall. The drag per unit surface area exerted upon the curved wall is roughly 70% of the drag per unit surface area upon the flat wall. Giving the greater extent of surface area for the curved wall, the difference regarding the drag value is negligible.
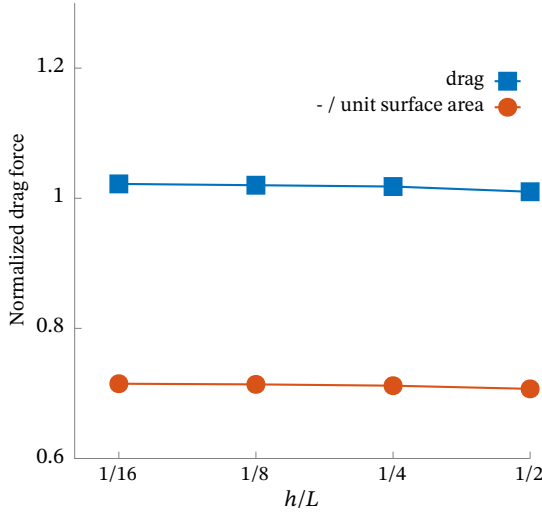
Figure A.15: Drag force and drag force per unit surface area exerted upon the curved wall of the microchannel normalized with respect to the drag force exerted upon the flat wall. The drag exerted upon the curved solid wall is almost equal to the drag exerted upon the flat wall, since the smaller drag per unite surface area is almost fully compensated by the greater surface area. .
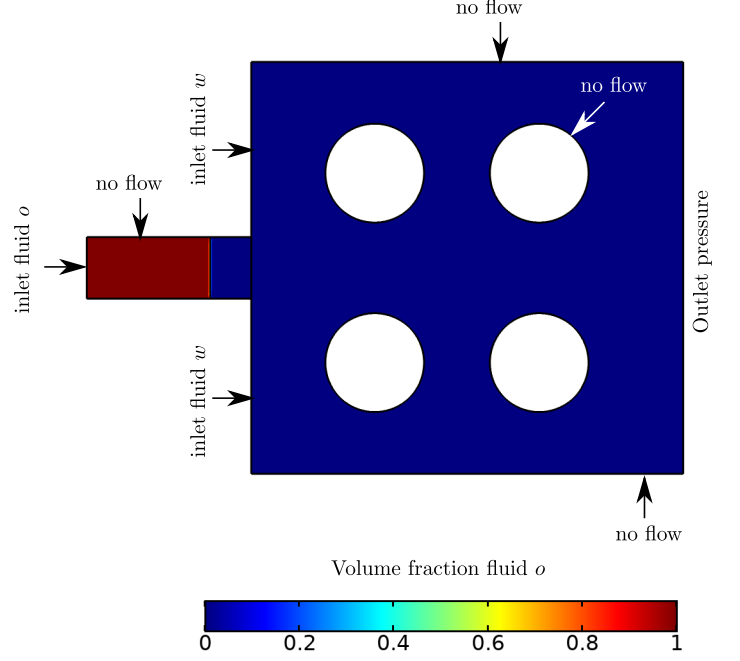

Figure B.16: Test case for comparison between Level Set and Boundary Element methods. The flow is cocurrent from left to right and the viscosity is the same for both fluids.

Appendix B.   Comparison with a Boundary Element Method

Here we validate the Level Set (LS) code by comparison with a Boundary-Element Method (BEM) [24], which relies on a surface discretization of the interface and a pseudo-analytical formulation in the bulk of the phases. This allows us to precisely locate the interface, even in the case of very thin film flow, and to carefully analyze the choice of parameters in Eq. 11.

The test case resembles the case study (Fig. B.16). The model is initially fully saturated with fluid w, with the exception of the channel through which fluid o is injected. We test either the $\phi = 0.5$ contour is an appropriate definition for the fluid-fluid interface and in what extent the value of the initialization parameter ψ can change the interface position. In Fig. B.17 we present the half-part of the model and the interface between the fluids at time $t = 2.5$, for an aspect ratio h/L, where L is the width of the fluid o inlet channel. We present three different interfaces obtained with the LS method, depending on the initialization parameter value. This parameter is normalized with respect to the inlet veloc-

ity of fluid o, which is three times greater than the fluid w inlet velocity. One can clearly observe that the interface position obtained with the LS method is almost identical to that obtained with the BEM, regardless of value of ψ. However, the best results, especially regarding the interface tip position, is obtained for $\psi = U_o^{\text{inlet}}$.
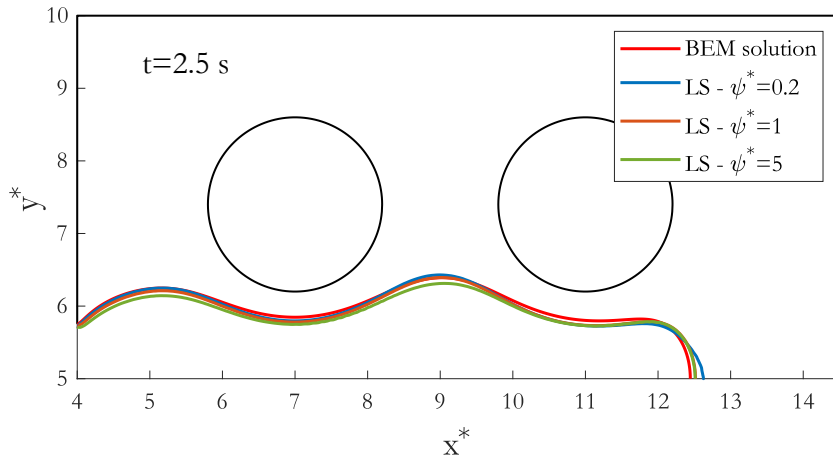
15

Figure B.17: Interface position at time $t = 2.5$ s obtained for an aspect ratio $h/L = 0.25$ with a Boundary Element method and the Level Set method for different values of the dimensionless initialization parameter $\psi^* = \psi/U_o^{\text{inlet}}$.